ASCE-ASME Journal of Risk and Uncertainty in Engineering Systems Part B: Mechanical Engineering
Online journal at:
asmedigitalcollection.asme.org/risk

# Bayesian Model Updating of Multiscale Simulations Informing Corrosion Prognostics Using Conditional Invertible Neural Networks

**Guofeng Qian**
Department of Structural Engineering,
University of California San Diego,
9500 Gilman Drive,
La Jolla, CA 92093-0085

**Jice Zeng**
Department of Industrial and Manufacturing
Systems Engineering,
University of Michigan-Dearborn,
Dearborn, MI 48128

**Zhen Hu**
Department of Industrial and Manufacturing
Systems Engineering,
University of Michigan-Dearborn,
Dearborn, MI 48128

**Michael D. Todd**[1]
Department of Structural Engineering,
University of California San Diego,
9500 Gilman Drive,
La Jolla, CA 92093-0085
e-mail: mdtodd@ucsd.edu

*Physics-based multiscale corrosion simulation plays a vital role in predicting the evolution of pitting corrosion on large civil infrastructure, contributing to a model-informed structural health monitoring strategy for risk-based asset health management. The physics-based analysis, however, may not accurately reflect the underlying true physics due to various uncertainty sources and needs to be updated using Bayesian inference methods based on observations to make the prediction closer to field observations. However, traditional Bayesian inference requires the evaluation of a likelihood function, which is often unavailable due to the complex model architecture and various surrogate models used in the analysis. Therefore, likelihood-free inference approaches are required for the updating of the multiscale corrosion simulation models. This paper meets this need by proposing a conditional invertible neural network (cINN)-based Bayesian model updating method for an existing corrosion simulation model. We first train a cINN model based on simulated observations generated from a high-fidelity forward corrosion analysis model. A convolutional neural network-based feature extraction algorithm is then employed to extract key features from corrosion images. After that, the extracted corrosion features are used as inputs of the cINN model to directly obtain posterior distributions of uncertain corrosion model parameters without evaluating the likelihood function. A case study of a miter gate structure is used to demonstrate the proposed approach. The results show that the proposed cINN-based model updating approach can provide more accurate inference results with a reduced computational cost in comparison to the classical approximate Bayesian computation (ABC) approach.* [DOI: 10.1115/1.4065845]

*Keywords: conditional invertible neural network, Bayesian model updating, structural health monitoring, multiscale simulation*

## 1 Introduction

Corrosion is a prevalent degradation mechanism in civil infrastructure, particularly for inland waterway structures such as dams and locks [1,2]. Among various degradation mechanisms, pitting corrosion stands out as the most detrimental, and may induce material loss, which eventually leads to component failure [3]. It is also worth noting that deep pits with sharp interfaces have the potential to trigger stress corrosion cracking [4–7]. However, localized pitting corrosion often is very difficult to detect until it significantly compromises structural integrity. Hence, it is imperative to develop reliable corrosion diagnostics and prognostics approaches. While significant efforts have been made in the past decades for corrosion diagnostics and prognostics of large civil infrastructure [8–13], accurately predicting corrosion evolution in a way that supports actionable information remains a challenge. This paper focuses on this prognostic function of pitting corrosion prediction, as opposed to in situ diagnostics of pitting corrosion.

Motivated by accurately predicting pitting corrosion evolution, various data-driven or empirical models have been proposed based on empirical datasets [14–18]. However, reliance on empirical data poses challenges due to its limited availability. Moreover, corrosion is influenced by factors such as mechanical load, temperature, and the electrochemical environment, making deterministic prediction challenging [19]. To address the various sources of noise or uncertainty in corrosion growth, stochastic models have been employed, characterizing model or input parameters as random variables represented by probability density functions like normal, lognormal, Weibull, and Gumbel [20–22]. A major limitation of these stochastic models, however, lies in their inability to properly account for uncertainties from various environmental sources. In contrast, physics-based prognostic models, including the finite volume method [23], cellular automata techniques [24], peridynamic formulations [25], and phase-field (PF) models [26], offer a

---

[1] Corresponding author.

Manuscript received May 20, 2024; final manuscript received June 19, 2024; published online September 26, 2024. Assoc. Editor: Chen Jiang.

more mechanistic understanding of corrosion. Among these, the PF method employs a continuous approach to represent phase change implicitly, enabling simulation of complex evolving morphology. However, various uncertainty sources, such as model parameter uncertainty and model form uncertainty, in these physics-based models may compromise their application in corrosion failure prognostics due to computational cost.

To reduce uncertainty sources during the long-term corrosion simulation process, Bayesian model updating is widely employed. This approach utilizes Bayes' theorem to infer the posterior distribution for model parameters based on the available data, and thus minimize disparities between observed and predicted responses. A key element in Bayesian model updating is the likelihood function, which assesses the probability of observing data given the forward predictive model and prior information [27,28]. However, for complex or physics-based models where the likelihood function is intractable, traditional Bayesian model updating methods become inapplicable. Different likelihood-free inference (LFI) approaches have been proposed to address challenges in parameter estimation when likelihood functions are unavailable. Beaumont et al. [29] introduced approximate Bayesian computation (ABC). By comparing simulated data generated from the model with observed data, parameter values that yield simulations resembling the observed data within a specified tolerance are accepted. It has been widely applied in various fields including genetics [29] and ecology [30]. Furthermore, Toni et al. [31] combine sequential Monte Carlo with ABC by iteratively updating a population of particles representing the posterior distribution through a series of importance sampling and resampling steps. Wood [32] proposed synthetic likelihood as an alternative to traditional likelihood-based inference, particularly suitable for complex models. It involves constructing a summary statistic of the data and using it to approximate the likelihood function. However, these likelihood-free inference methods face two challenges: assessing the discrepancy between observed and simulated data [33] and the computational cost associated with generating a large number of simulations due to the unknown relation between model parameters and discrepancies.

With the development of machine learning and deep generative learning algorithms, normalizing flow implemented by conditional invertible neural network (cINN) has emerged as a powerful tool for probabilistically solving inverse problems [34]. Normalizing flow is a class of methods used in machine learning to transform simple probability distributions into more complex ones using a sequence of invertible and differentiable transformations [35]. By starting with a simple, known distribution and applying these transformations, a normalizing flow can create highly flexible distributions that can effectively capture intricate data patterns. Compared to classical LFI algorithms, cINN has the advantage of directly approximating the posterior distributions for given observations without evaluating the likelihood functions. This unique feature allows cINN to bypass the computationally expensive simulation process required in classic LFI approaches. The cINN has been applied to different areas including image generation [36], physical parameters inference [37], updating empirical/statistical degradation models [38,39], and other inverse problems [40]. Considering these advantages of cINN, this paper investigates Bayesian model updating of a physics-based multiscale corrosion simulation using cINN-based likelihood-free inference approach. It enables real-time Bayesian model updating of the complex corrosion simulation models, which is essential for online structural health monitoring. Results of a practical application show that inference based on cINN is more accurate than the previous method with a significantly reduced computational cost. The main contributions of this paper can therefore be summarized as:

- A model updating framework for a multiscale corrosion simulation model using synthetic images.
- Integration of the cINN model with the multiscale corrosion simulation model to efficiently perform model updating.
- Comparison of the cINN-based corrosion model updating method with the classical ABC method.
- Real-world application of the proposed framework to miter gates, which is a type of inland waterway civil infrastructure.

The remainder of this paper is organized as follows. Section 2 introduces the background of multiscale simulation. Section 3 describes the feature extraction process from corrosion images. Section 4 elaborates details of Bayesian inference with a cINN. Sections 5 and 6 present the results and discussions.

## 2 Background: Multiscale Corrosion Simulation and Modeling Updating

A multiscale corrosion simulation framework developed in our previous research is employed in this paper to maintain fidelity of the simulation while effectively managing the computational cost [41,42]. This simulation framework implements a hybrid model architecture to address stages where the corrosion mechanisms are not comprehensively understood by physics-based modeling. As shown in Fig. 1, the multiscale corrosion simulation model used in this paper is comprised of three main components:

- A multiphysics single pit simulation
- A statistical pit initiation simulation
- A physics-based structural analysis

The single pit simulation captures the evolution of an individual pit under varying mechanical stress and other environmental factors. Given the ongoing research on pit initiation mechanisms, a statistical initiation model is employed to simulate the initiation of multiple pits. Subsequently, a finite element (FE) structural analysis model is utilized to ascertain the global stress response of the structure. The local stress response is then employed as the mechanical load for the local evolution of multiple pits. In what follows, we provide a brief overview of each component of the multiscale simulation framework.

**2.1 Multiphysics Single Pit Simulation.** A multiphysics single pit simulation is employed to model the single pit evolution. It considers the influence of mechanical stress on the corrosion evolution by coupling the mechanical term into electrochemical equations as described in the literature [11]. The coupled partial differential equations are implemented with PF method to determine the pit growth.

The mechanical influence is coupled into the corrosion potential by a mechanical potential $\mu_{\mathrm{me}}$ in mechanochemistry as shown in the following equation by Gutman [43,44]:

$$\mu_{\mathrm{me}} = \int_{P_1}^{P_2} v(P)\, dP \approx \Delta P V_m \tag{1}$$

where $\mu_{\mathrm{me}}$ represents the mechanical influence on corrosion potential, $P_1$ and $P_2$ are the initial pressure, and $V_m$ is the molar volume. With the capability to evaluate the influence of the mechanical stress, the model, $\Phi(\cdot)$, can simulate the pit evolution under altering mechanical load $s_{0:t}$ and electrochemical environment characterized by the reaction coefficient, $\theta$, during the service. The pit morphology at a future time $t$ can be obtained as (see illustration in Fig. 1)

$$\omega_t = \Phi(s_{0:t}, \theta, \omega_0) \tag{2}$$

where $\omega_t$ represents the pit morphology at time $t$, $\Phi(\cdot)$ represents the multiphysics pit corrosion simulation, and $\omega_0$ represents the initial pit morphology at $t_0$.

While this model provides detailed pit evolution information, the initiation process has not been modeled. The pit initiation time and location modeling will be introduced next.

**2.2 Statistical Pit Initiation Simulation.** The pit initiation process is still an active research area [45–48]. The detailed

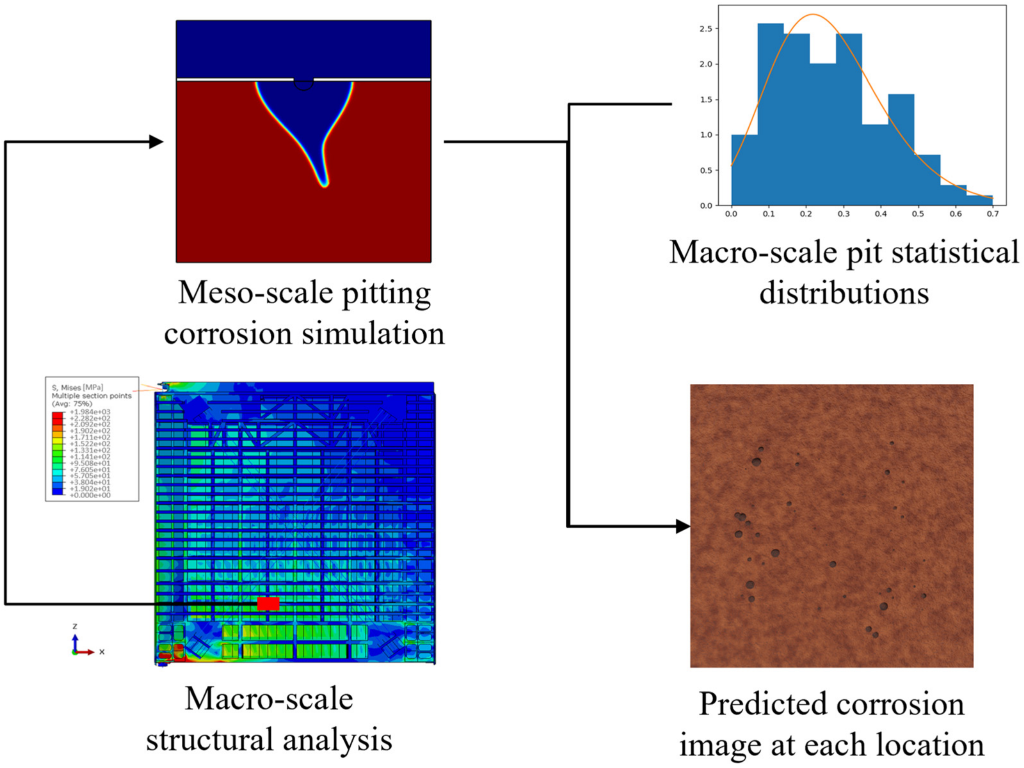

**Fig. 1 The physics-based multiscale corrosion simulation**

mechanism of the influence from stress is not well understood [46,49,50], such that the influence from stress on pit initiation is not considered. Therefore, we describe the pit initiation time and location by statistical information. The Poisson process is applied because the randomness of the passive film breakdown event. Multiple experimental results [51,52] also validated that the pit initiation time follows the Weibull distribution very well. In this paper, the pit initiation time is modeled as a Weibull distribution as below

$$T_{\mathrm{ini}} = F(\lambda, \beta) \tag{3}$$

where $T_{\mathrm{ini}}$ represents the pit initiation time and $\lambda, \beta$ are, respectively, the shape and scale parameters of the Weibull distribution.

**2.3 Physics-Based Structural Analysis.** A high-fidelity FE model was built for stress analysis and validated with strain measurements [53] on the Greenup navigational locks (see Fig. 2). The main mechanical load is from the hydrostatic pressure under changing water elevations from both sides. The dimension of the gate is about $63 \times 61$ feet.

The FE model of the gate is discretized into 64,919 elements in ABAQUS. The gate is primarily composed of thin steel elements so the FE model applies 3D shear elements. The beam-column elements are used for the diagonals and anchor bars. The four-node, reduced integration linear quadrilateral elements are primarily used and three-node full-integration linear triangular elements for complex geometry. This FE model is able to simulate the stress response at every location on the gate [54]. The local stress response would provide the mechanical load $s_{0,t}$ to the single pit growth simulation discussed in Sec. 2.1. It is essential to note that the stress response of the miter gate structure resulting from stable water elevation changes is treated as quasi-static while the changing load is considered as dynamic in the long-term corrosion simulation process.

More detailed information about the multiscale pitting corrosion simulation framework can be found in Ref. [41].

**2.4 Bayesian Model Updating of the Multiscale Corrosion Simulation Model.** Due to the changing environmental loading conditions, we applied Bayesian model updating to make sure that the model adapt to the changing circumstances. Bayesian model updating enables the seamless integration of new data into existing models, accommodating uncertainty while incorporating prior knowledge. It can also facilitate informed decision-making, making it a vital tool for life-cycle optimal maintenance.

Three key parameters in the model, namely, $\lambda$, $\beta$ for pit initiation, and $\theta$ for pit propagation, are updated for the multiscale model. These parameters are chosen due to their sensitivity to environmental uncertainties, while also being not directly measurable. While stress is also a crucial parameter, strain measurements have demonstrated practicality and accuracy in previous studies [53].

**Fig. 2 Greenup miter gate in inland waterway system**

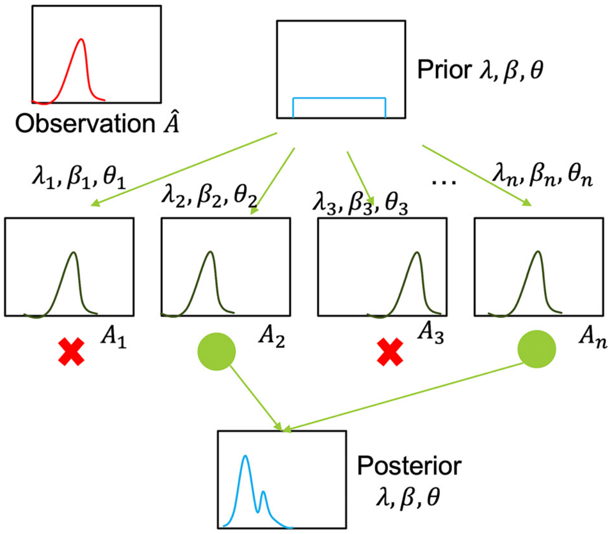

**Fig. 3 Illustration for ABC process [30]**

Given the local nature of the pitting corrosion, image observations are employed for model updating considering its advantage in economic cost and flexibility of noncontact sensing. Bayesian model updating from image observation $\mathbf{O}$ can be iteratively performed as

$$f(\lambda, \beta, \theta|\mathbf{O}) = \frac{\mathcal{L}(\mathbf{O}|\lambda, \beta, \theta)p(\lambda, \beta, \theta)}{\int\int\int \mathcal{L}(\mathbf{O}|\lambda, \beta, \theta)p(\lambda, \beta, \theta)d\lambda d\beta d\theta} \tag{4}$$

where $\mathcal{L}(\mathbf{O}|\lambda, \beta, \theta)$ represents the likelihood function of observing $\mathbf{O}$ for given model parameters $\lambda, \beta$, and $\theta$, and $p(\lambda, \beta, \theta)$ is the prior distribution of the uncertain model parameters.

More specifically, in this study, the pit width at the surface $A_t$ is selected as the observational feature from the image observation $\mathbf{O}_t$ to update the model because the width can be directly measured from an image. Notice that the pit number $N_t$ can also be computed based on the information of length $A_t$ of different pits in an image. The process of extracting $A_t$ from an image can be denoted as

$$\hat{A}_t = \Xi(\mathbf{O}_t) \tag{5}$$

where $\Xi$ represents the convolutional neural network-based feature extraction algorithm extracting the pit width $\hat{A}_t$ from an image. The detailed algorithm for this feature extraction can be found in our previous paper [55].

**2.5 Existing Method for Multiscale Corrosion Model Updating and Its Limitations.** As mentioned previously, deriving an analytical solution of the likelihood function for the multiscale corrosion simulation model is very challenging due to (1) the complex model architecture; (2) the complicated feature extraction process; and (3) the usage of different types of surrogates to accelerate the simulations. LFI method is preferred to solve the Bayesian model updating problem given in Eq. (4).

Multiple likelihood-free approaches have been proposed for complex models [29,32,56,57]. The shared idea is to identify model parameters by finding outputs from simulations similar to those from observations. Among them, ABC has been applied for multiscale corrosion model updating [55]. Figure 3 illustrates the ABC process. As depicted in this figure, several samples from the prior distribution of $\lambda, \beta, \theta$ are incorporated into the multiscale pitting corrosion simulation. Subsequently, the observable feature, pit width $A_{it}$ of the $i$th sample, is juxtaposed with the observation $\hat{A}_t$. Following this comparison, the $i$th sample will be included in the posterior sample set if the difference between $A_{it}$ and $\hat{A}_t$ falls within the predetermined threshold. Then, an approximation of the posterior distribution will be derived based on the accepted samples.

However, due to the characteristics of the multiscale simulation, we split the original ABC approach into two stages to fit the simulation as shown in Algorithm 1. First, the shape and scale parameters, $\lambda, \beta$, describing the pit initiation time are updated with the number of pits $\hat{N}_t$ as the pit initiation time is reflected in the number of pits instead of the pit width. Second, the reaction coefficient $\theta$ is updated with the pit width distribution, $\hat{A}$, because the pit width is directly related to the reaction coefficient. The simulation results at two stages are compared with the observations. Samples within the threshold are kept as posterior samples. The general steps are shown in Algorithm 1. Generally, stage 1 uses the pit number identified to infer two parameters controlling pit initiation and stage 2 uses pit width distribution identified to infer reaction constant in pit propagation.

**Algorithm 1** Inference with ABC for multiscale corrosion model updating

```
Stage 1: Randomly draw 1000 samples $\lambda_i, \beta_i$ from prior uniform distribution to simulate pit initiation time $T_i$
for $i = 0$ to 1,000 do
    Compute the number of pits $N_{ti}$
    Compare that number with observation $\hat{N}_t$
    Reject samples with large accumulated distance between $N_{ti}$ and $\hat{N}_t$
end
Approximate the posterior distribution from remaining samples with kernel density estimation
Stage 2: Draw 500 samples of $\lambda_j, \beta_j$ from the posterior distribution from stage 1 and combine with 500 samples of $\theta_j$ from a uniform distribution as a prior for stage 2
for $j = 0$ to 500 do
    Simulate each pit growth with surrogate model
    Approximate the PDF of pit radius distribution at each time as $A_{tj}$
    Reject samples with large accumulated distance between $A_{tj}$ and $\hat{A}_t$
End
Approximate the posterior distribution from remaining samples
```

The process of generating the posterior distribution typically necessitates hundreds of evaluations, leading to hours of computing time for the inference process. In our study, we conducted evaluations for 1,000 samples in stage 1 and 500 samples in stage 2. This discrepancy in sample size is due to the lower computational cost in stage 1 compared to stage 2. The inference results will be detailed in Sec. 5 for reference. The number of samples is determined by balancing the computational cost and the need for a sufficient quantity to estimate the posterior distribution in stage 2. In this study, two hundred samples are used for this purpose. However, the number of samples required at each stage relies on human judgment, which might introduce uncertainties into the model updating process. It is worth noting that the posterior distribution can be significantly influenced by the threshold value, yet there is currently no standardized approach for setting this value. Therefore, there is a pressing need for the development of more efficient and robust inference methods.

## 3 Convolutional Neural Network-Based Feature Extraction From Images

As mentioned previously, pit width serves as the primary damage feature selected for updating the pitting corrosion analysis model since that information can be directly extracted from image observations. Image observation presents a convenient and cost-effective method for assessing local surface damage, such as pitting corrosion [58,59]. However, due to the gradual nature of corrosion, it often takes years for significant changes to become apparent, rendering longitudinal inspection data over extended periods unavailable. To circumvent this limitation and test the efficacy of the proposed method in this paper, we leverage advancements in computer graphics to generate synthetic image data. Specifically, we develop a graphic model of a plate as an example using BLENDER software and incorporate textures derived from real corrosion images to simulate realistic pitting corrosion scenarios. The evolution information for the graphic model comes from the physics-based simulation described in Sec. 2. The pit dimension is modified with random noise to mimic the stochastic nature of the corrosion process.

We follow the procedures outlined in Fig. 4 to extract information of pit width. Initially, the graphic model renders the plate at various angles and time points to generate synthetic corrosion images, simulating the process of capturing photographs. Subsequently, the synthetic observation images undergo pixel-level corrosion identification using a pretrained U-net network, as indicated by the left arrow. The architecture of this network is depicted at the bottom of Fig. 4. Based on the binary identification result, morphological closing techniques are employed to address any remaining areas among overlapping pits. The pit width is then determined using distance transform, with the identified width denoted as $\hat{A}_t$. The scaling factor is determined based on a reference point on the model. Further details can be found in Ref. [55]. The identified pit width is subsequently used to update the forward corrosion simulation model.

While we acknowledge that there may be differences between the pictures generated in the graphical Blender model and those captured by a camera, our proposed convolutional neural network-based identification and feature extraction algorithm remain applicable once actual images are available. This algorithm is designed to effectively identify and extract relevant features from images, regardless of minor variations in image quality or appearance.

## 4 Likelihood-Free Inference with Conditional Invertible Neural Networks

The approach of leveraging a cINN for likelihood-free inference in estimating posterior distributions marries the principles of Bayesian inference with the power of deep learning. At its core, this method employs a normalizing flow, a transformative process that bridges the gap between complex, non-Gaussian distributions (such as posterior distributions) and simpler, multivariate Gaussian distributions. One of the key strengths of a normalizing flow is its scalability, which allows it to adeptly handle distributions ranging from straightforward, low-dimensional forms to intricate, high-dimensional ones.

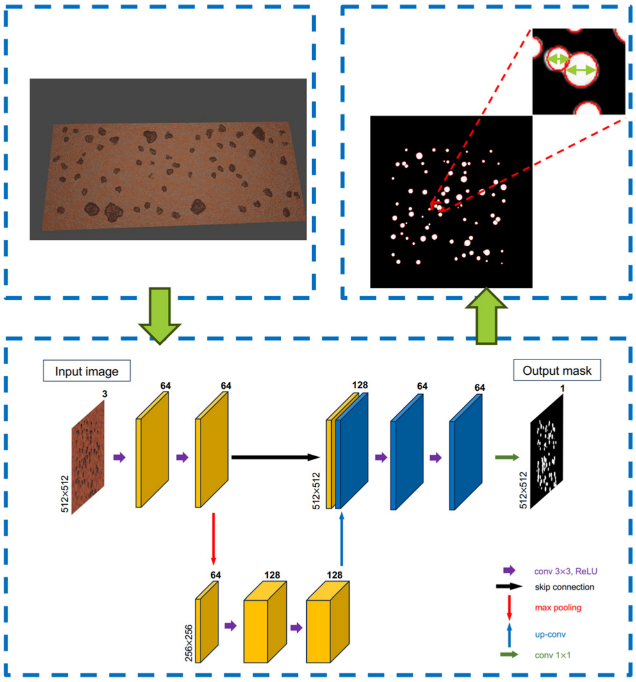

Fig. 4 The feature extraction procedure from graphic model

Illustrated in Fig. 5, the normalizing flow framework features two primary pathways: the generative direction and the normalizing direction. In the generative aspect, the process begins by sampling a latent variable $z_0$ from a basic distribution $p_z(z_0)$ and subsequently engages in an iterative procedure to find $z_i = L_i(z_{i-1})$, thereby generating samples of model parameters $\Omega = \{\lambda, \beta, \theta\}$ via an invertible function $L(\cdot)$. Conversely, in the normalizing pathway, a function $h(\cdot)$, which represents the inverse of $L(\cdot)$, is employed to transform the posterior distribution back into a simple Gaussian form.

Building on this framework, the method defines that for a given set of observations $A_{o,1:k} = \{A_{o,1}, A_{o,2}, \ldots, A_{o,k}\}$ spanning from time-step $t_1$ to $t_k$, the posterior distribution may be effectively approximated [60] as

$$p(\theta|A_{o,1:k}) = p_z(z)\left|\det\left(\frac{\partial h(\Omega)}{\partial \Omega}\right)\right| = p_z(z)\left|\det\left(\frac{\partial L(h(\Omega))}{\partial z}\right)\right|^{-1} \tag{6}$$

In practical applications, constructing complex invertible functions $L(\cdot)$ for nonlinear bijective mapping presents challenges. This study employs a series of conditional affine coupling layers (cACLs) [61] to establish a cINN for the realization of normalizing flow. A cINN is characterized by its ability to invertibly transition from a simple probability density to a more complex one through a sequence of invertible structures. For this bijective mapping, a latent variable with an easy-to-sample density is crucial, as it enables the inference of model parameters from the latent space based on observations in the reverse mapping, as depicted in Fig. 5. Furthermore, this research introduces a summary network alongside the cINN to address the challenge of handling measurement sequences of variable length, similar to Ref. [60]. More critically, the summary network is designed to distill the most informative features directly from measurements contaminated with noise. In the approach to flow-based likelihood-free inference presented here, the inference network-implemented via the cINN and the summary network are integrated and trained in a unified manner. This trained cINN framework then performs inverse evaluation of the forward model, leveraging summarized information derived from the summary network to infer parameters.

The summary network and cINN are denoted as $\mathcal{H}$ and $\mathcal{F}$, respectively. The time series measurement $A_{o,1:k}$ undergoes filtering and is then processed by $\mathcal{H}$ to extract informative statistics, represented as

$$\tilde{A}_k = \mathcal{H}(A_{o,1:k}; \alpha_s) \tag{7}$$

where $\tilde{A}_k$ denotes compressed, fixed-size vectors that contain sufficient statistics throughout the measurement period. The term $\alpha_s$ refers to the hyperparameters within the summary network. Following this, samples approximating the posterior distributions are generated by sampling $z$ given the summarized information $\tilde{A}_k$, as depicted through the generative process in Fig. 5

$$\hat{\Omega}^{(i)} = \mathcal{F}^{-1}(\tilde{A}_k, z^{(i)}; \alpha_c), \quad i = 1, \ldots, N_{\mathrm{MCS}} \tag{8}$$

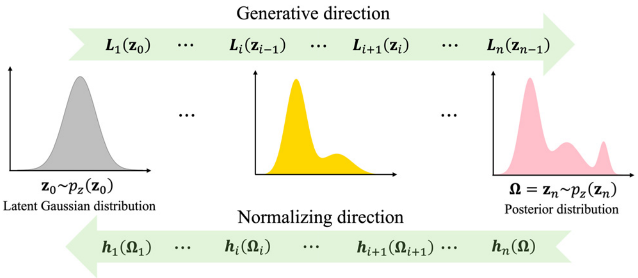

Fig. 5 The concept illustration of normalization flow

where $z^{(i)}$ is the $i$th sample of the latent variable $z$, following a normal distribution $N(0, I)$. $\tilde{A}_k$ is derived from Eq. (7). The term $\alpha_c$ denotes the hyperparameters in the cINN and $N_{\text{MCS}}$ is the total number of samples. The hyperparameters $\alpha_s$ and $\alpha_c$ in the two complementary deep neural networks are optimized together during the training phase. If we define a parameter vector $\phi = \{\alpha_s, \alpha_c\}$ that encompasses all network hyperparameters, the optimal $\hat{\phi}$ can be determined by minimizing the Kullback–Leibler divergence between the target posterior $p(\Omega|A_{o,1:k})$ and the approximate posterior $p_\phi(\Omega|A_{o,1:k})$ [60]

$$\begin{aligned}\hat{\phi} &= \arg\min_{\phi} \mathbb{E}_{p(A_{o,1:k})}[\mathrm{KL}[p(\Omega|A_{o,1:k}) \parallel p_\phi(\Omega|A_{o,1:k})]] \\ &= \arg\max_{\phi} \mathbb{E}_{p(A_{o,1:k},\theta)}[\log p_\phi(\Omega|A_{o,1:k})] \end{aligned} \tag{9}$$

where $\mathrm{KL}[p \parallel p_\phi]$ is the Kullback–Leibler divergence and $\mathbb{E}(\cdot)$ is the expectation operator.

During the offline training phase, we generate synthetic data $A_{\text{sy},1:k}$ to train the inference model, utilizing the prior knowledge of model parameters from a forward model. The expectation in Eq. (9) is approximated using Monte Carlo simulations with the synthetic observations

$$\hat{\phi} = \underset{\phi}{\operatorname{argmax}} \left\{ \frac{1}{N_{\text{syn}}} \sum_{i=1}^{N_{\text{syn}}} \left( \log p_\phi \left( \Omega^{(i)}; \tilde{A}^{(i)}_{\text{sy},1:k} \right) + \log \left| \det J^{(i)}_{p_\phi} \right| \right) \right\} \tag{10}$$

where $\tilde{A}^{(i)}_{\text{sy},1:k} = \left\{ \tilde{A}^{(i)}_{\text{sy},1}, \tilde{A}^{(i)}_{\text{sy},2}, \ldots, \tilde{A}^{(i)}_{\text{sy},k} \right\}$ represents the compressed and informative data obtained from the summary network. $J_{p_\phi}$ denotes the Jacobian matrix of $p_\phi$, computed as $(\partial p_\phi(\Omega; \tilde{A}^{(i)}_{\text{sy},1:k})/\partial\Omega)$. The entire neural network in cINN is designed to be invertible, which allows for an efficient computation of the Jacobian determinant. This efficiency arises from the network's formulation, which ensures that the Jacobian is structured as either an upper or lower triangular matrix, rendering the evaluation process cost-effective [60]. The ultimate training goal for both networks is given by

$$\hat{\phi} = \underset{\phi}{\operatorname{argmin}} \left\{ \frac{1}{N_{\text{syn}}} \sum_{i=1}^{N_{\text{syn}}} \left( \frac{||p_\phi \left( \Omega^i; \tilde{S}^{(i)}_{\text{sy},1:k} \right)||_2^2}{2} - \log \left| \det J^i_{p_\phi} \right| \right) \right\} \tag{11}$$

Equation (11) can be solved via any stochastic gradient descent method, ensuring that the networks are capable of accurately estimating the precise posterior distribution (given ideal convergence). For a detailed mathematical derivation, refer to Ref. [60].

The procedures for inference using cINN are detailed in Algorithm 2: and encompass three primary steps:

(1) **Synthetic Data Generation**: Synthetic data, denoted as $A_{\text{syn},1:k}$, representing pit growth over $k$ time steps, are produced. These data are generated based on a uniform prior distribution of the model parameters $\Omega$, utilizing a physical model.
(2) **Offline Network Training**: The synthetic data are input to the summary network, followed by the inference network. Both networks are trained concurrently, with their parameters updated according to Eq. (11).
(3) **Online Posterior Sampling**: After achieving convergence of the hyperparameters, posterior samples are generated. This is accomplished by drawing samples from the latent Gaussian distribution and applying the learned inverse transformation. Specifically, observed or test data are fed into the trained summary and inference network to obtain these samples.

**Algorithm 2** Inference with a cINN for multiscale corrosion model updating

```
Synthetic data generation: Generate 500 samples of $\Omega = \{\lambda, \beta, \theta\}$ from a uniform prior distribution to simulate the pit growth data $A_{\text{syn},1:k}$ for $k$ time steps, giving training pairs as $\{\Omega, A_{\text{syn},1:k}\}$.
Offline Network Training
  • Pass the synthetic data $A_{\text{syn},1:k}$ to the summary network: $\tilde{A}_{\text{syn},1:k} = \mathcal{H}(A_{\text{syn},1:k}; \alpha_s)$
  • Pass the pairs $\{\Omega, \tilde{A}_{\text{syn},1:k}\}$ to the inference network (cINN) in the forward direction: $z = \mathcal{F}(\Omega, \tilde{A}_{\text{syn},1:k}; \alpha_c)$
  • Compute the loss using training data $\{\Omega, \tilde{A}_{\text{syn},1:k}, z\}$ by Eq. (11)
  • Update hyperparameters $\{\alpha_s, \alpha_c\}$ in neural networks via stochastic gradient descent
Online posterior sampling
  • Pass the observed data $A_{o,1:k}$ to the trained summary network: $\tilde{A}_{o,1:k} = \mathcal{H}(A_{o,1:k}; \alpha_s)$
  • Sample latent variables $z^{(i)} \sim N(0, I)$, for $i = 1, \ldots, N_{\text{MCS}}$
  • Pass $\{\tilde{A}_{o,1:k}, z\}$ to the trained inference network in the inverse direction: $\Omega^{(i)} = \mathcal{F}^{-1}(\tilde{A}_{o,1:k}, z^{(i)}; \alpha_c)$
  • Collect all samples $\Omega^{(i)}$ for target posterior $p(\Omega|A_{o,1:k})$
```

## 5 Application to Corrosion Prognostics for Miter Gates

**5.1 Corrosion in Miter Gates.** Miter gates, as shown in Fig. 2, serve as crucial components within inland waterway navigation networks, facilitating the passage of watercraft between different water elevations along the waterway. These metallic structures play a vital role in maintaining navigational efficiency and ensuring safe transit for vessels. In the U.S. alone, there are over two hundred navigational locks, with over half of them having been in operation for more than 50 years as of 2017. This underscores the importance of ensuring the reliability and structural integrity of miter gates to sustain the functionality of inland waterway transportation systems [62].

The susceptibility of miter gate structures in navigational locks to corrosion is primarily attributed to prolonged exposure to water and debris. Despite preventive measures such as paint protection and the use of sacrificial zinc anodes on newer gates, corrosion remains a persistent issue. The leftmost images in Fig. 6 depict corrosion occurring beneath the paint layer. In the middle images, severe corrosion is evident at the bottom of the gate, as observed at Overton lock. The rightmost images highlight extensive corrosion on a retired gate, underscoring the significant challenges posed by corrosion in maintaining the structural integrity of miter gates.

Pitting corrosion is regarded as particularly hazardous for several reasons [3]. First, its localized nature makes it challenging to detect, especially in structures such as miter gates where a significant portion is submerged underwater. Inspecting these underwater sections either requires specialized workers to dive into the water, which poses significant safety risks, or the entire lock to be shut down and dewatered, incurring substantial expenses. Minimizing downtime is crucial due to the considerable economic losses incurred when goods are unable to be transported. Second, pitting corrosion has the potential to cause significant damage by initiating stress corrosion cracking [63]. In miter gate structures, which constantly experience fluctuating hydrostatic pressures within the lock during each operational cycle, the repeated loading enhances the likelihood of crack initiation and propagation. Therefore, it is imperative to address pitting corrosion before it progresses to the point of crack initiation.

**5.2 Training of the Accelerated Multiscale Model.** The phase-field simulation takes dynamic (for corrosion process) stress response from the FE structural analysis. One group of simulation results is shown in Fig. 7. The time scale of PF simulation is calibrated to 10 years with 200 time steps.

As mentioned in Sec. 2, the multiphysics PF simulation in the multiscale forward model contains multiple coupled partial differential equations. The average computing time is more than

Fig. 6 Corrosion on miter gates

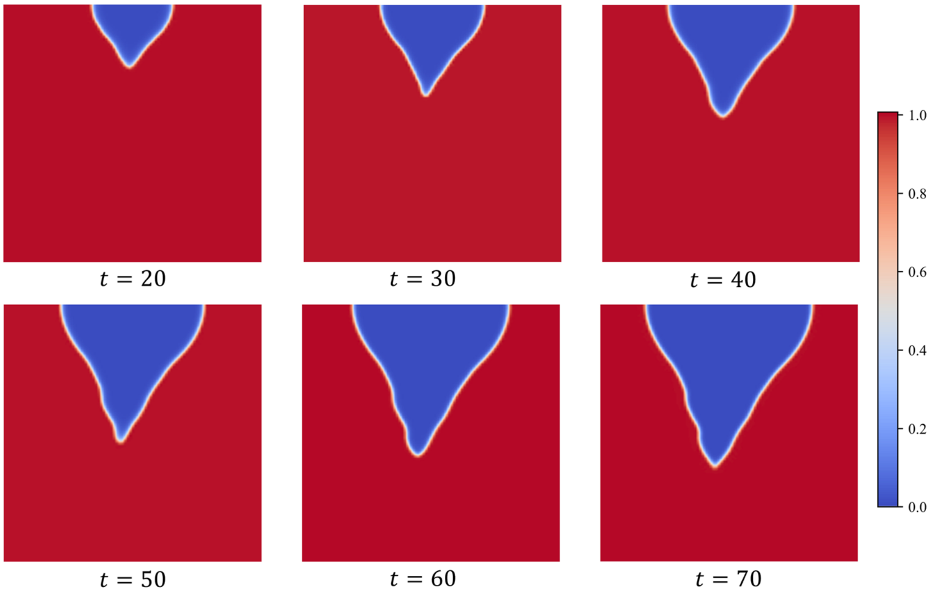

Fig. 7 Phase-field simulation under dynamic stress load

an hour on a workstation with 10 cores of an Intel(R) Xeon(R) W-2155 CPU. To accelerate this simulation, we developed a Gaussian process regression model with a nonlinear autoregressive exogenous (NARX) inputs to predict three key features of the pit morphology including pit width, pit depth, and the curvature at the tip location. Two hundred simulations with different dynamic load inputs as well as reaction coefficients $\theta$ are performed to generate training data. Details of this GP-NARX model can be found in Ref. [55]. One typical multistep prediction result is shown in Fig. 8.

The depth prediction results are accurate except for the last 20 time steps. The pit width prediction is also accurate with a certain level of prediction uncertainty, while the curvature prediction is not accurate and contains lots of uncertainties due to complex growth mechanism of curvature at the tip location. The pit width growth surrogate model is used as part of the multiscale model to be updated. The pit depth growth surrogate is used to perform prognostics for depth growth after the multiscale model is updated. A Gaussian process regression surrogate for the structural analysis FE model is used such that all parts of the multiscale simulation can be accelerated. After the employment of different types of surrogates, the accelerated multiscale simulation takes seconds to run. Overall, the surrogate model is used because fast/real-time prediction is desired in the Bayesian model updating and online prognostics.

### 5.3 Training of the Conditional Invertible Neural Network Model.

Three key parameters, $\lambda, \beta$, and $\theta$ in the multiscale simulation introduced in Sec. 2 are selected to be inferred with image observation introduced in Sec. 3. 500 samples are used in the training process for the cINN-based method, which is the same number of samples needed in the stage 2 of the ABC approach. Since the cINN can perform inference from both the pit number and the pit width distribution together, it does not require a two-stage structure during the training process. Furthermore, the proposed cINN-based

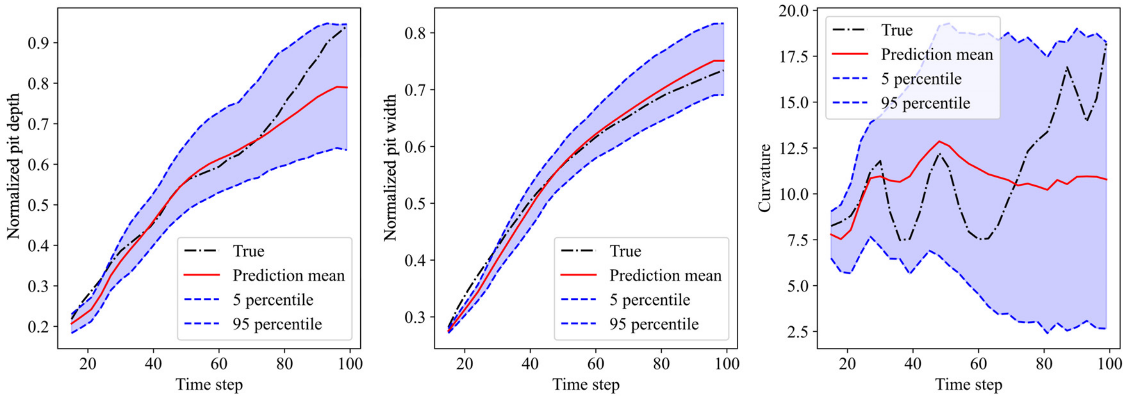

Fig. 8 Features prediction results from GP-NARX model

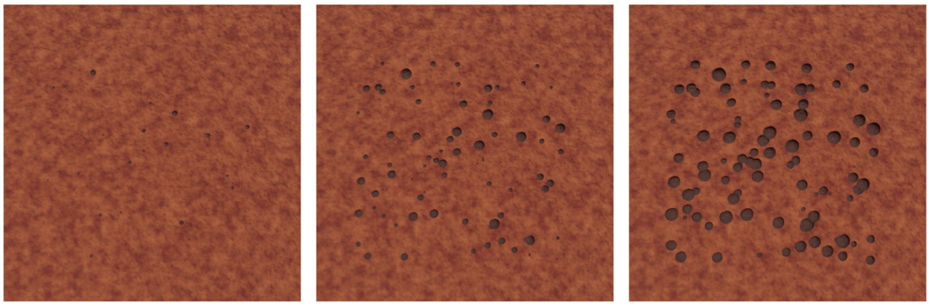

$t = 50$ $t = 100$ $t = 150$

Fig. 9 Observation images at different time steps

method does not rely on a "reject-accept" mechanism to infer posterior samples, thereby eliminating the need for a similar two-stage structure as used in the ABC approach during the inference process as well. Similar to inference with ABC introduced in Sec. 2, 500 samples of three parameters from prior uniform distribution are evaluated with the accelerated multiscale simulation as no prior information is assumed. These samples and evaluation results serve as the training data for the summary network and inference network implemented by cINN, introduced in Sec. 4. For the summary network, we employ a 1D convolutional architecture with kernel sizes of 64, 64, 128, and 128. The activation function used is ReLU, and a dropout rate of 0.5 is implemented to prevent overfitting. The output is ultimately compressed into a fixed 256-dimensional vector. The inference network is designed to consist of 12 cACLs with four fully connected internal networks, ensuring sufficient depth in the network architecture. The initial learning rate is set at 0.001, with a decay rate of 0.95. Both the summary and inference networks are trained simultaneously on 480 training samples over 100 epochs, with each epoch comprising 50 iterations. The remaining data are used for validation purposes.

It is worth mentioning that in this study, we did not extensively fine-tune the hyperparameters of the cINN model. The most crucial hyperparameter in the cINN model is the number of cACLs stacked sequentially to construct the inference network cINN. According to the literature [60], 5–12 cACLs are generally sufficient for most scientific problems. Therefore, we adopted 12 cACLs in this study to ensure the model's expressiveness. For the implementation of the cINN, the model was trained on a MacBook Pro 2017 with a 3.1 GHz Dual-Core Intel Core i5 processor. The environment was setup with Python 3.6 and TensorFlow 1.3 for the training process. The deep learning framework employed is the open-source package available at BayesFlow GitHub repository, which provides the necessary tools and functions to build and train our cINN model efficiently.

**5.4 Inference and Prognostics Results.** The same observations, as shown in Fig. 9 as ABC examples, are used to test the effectiveness of cINN inference approach. For both ABC and cINN, images from first 165 time steps are used as the observations for inference and the next 35 time steps will be predicted based on the inference result.

The mean values for posterior distributions obtained from cINN and ABC are shown in Table 1. The mean value of posterior distribution of $\lambda$ for both approaches are very close to the reference value. cINN approach is a little bit more accurate in inferring $\beta$. The mean values of $\theta$ for both approaches deviates from the reference value and ABC approach has more accurate prediction of $\theta$. However, the variance values of cINN approach are much smaller than those of the ABC approach. The mean values from ABC are closer to mean of the prior distribution than their counterparts from cINN.

Figure 10 shows the detailed posterior probability density function (PDF) surface of three parameters after inference. The reference values for $\lambda$, $\beta$, and $\theta$ are shown as dashed line in each plot. The first row shows the posterior PDF inferred with cINN approach and the second row shows the posterior PDF inferred with ABC approach. The $z$-axis represents the joint probability density and the $x$,$y$ axis represents two parameters among three. Overall, the posterior distributions of cINNs are more concentrated than those of ABC. The maximum probability density for each joint PDF is also higher. All of three joint PDF surfaces of the cINN have bell-shaped curve with one single peak. But for joint PDF surfaces of $\lambda$, $\beta$ and $\beta$, $\theta$ in ABC, there are multiple peaks and irregular PDF surfaces. Although mean value of ABC posterior for $\theta$ is closer to the

Table 1 Means and standard deviations of posterior distribution after inferences

| | Mean | Standard deviation |
|---|---|---|
| Prior | (3, 3, 5.5) | (1.33, 1.33, 6.75) |
| cINN | (1.94, 2.08, 7.57) | (0.18, 0.12, 0.50) |
| ABC | (2.10, 2.91, 6.84) | (0.92, 0.89, 2.22) |
| Reference | (2, 2, 5) | (0, 0, 0) |

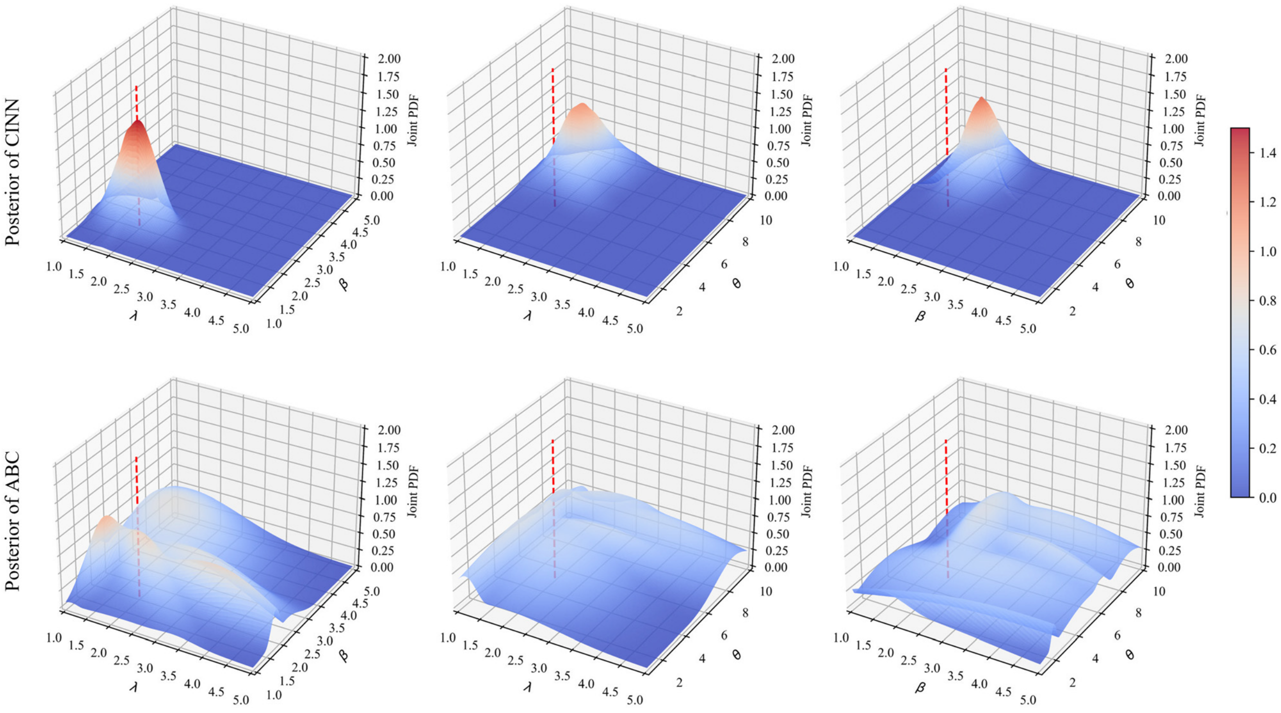

Fig. 10 Posterior PDF of three key parameters after inference from ABC and cINN

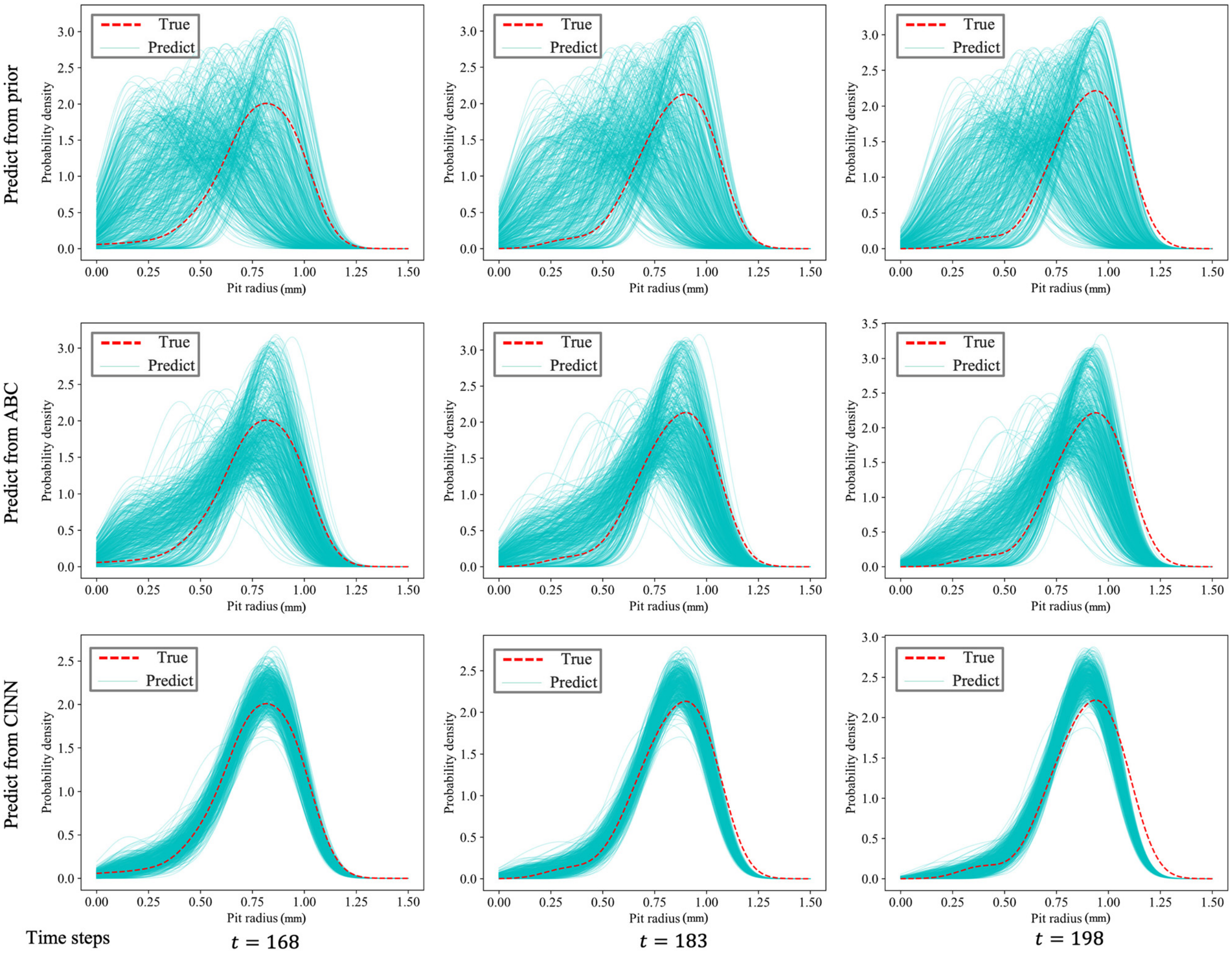

Fig. 11 Width prediction results from the updated corrosion model parameters

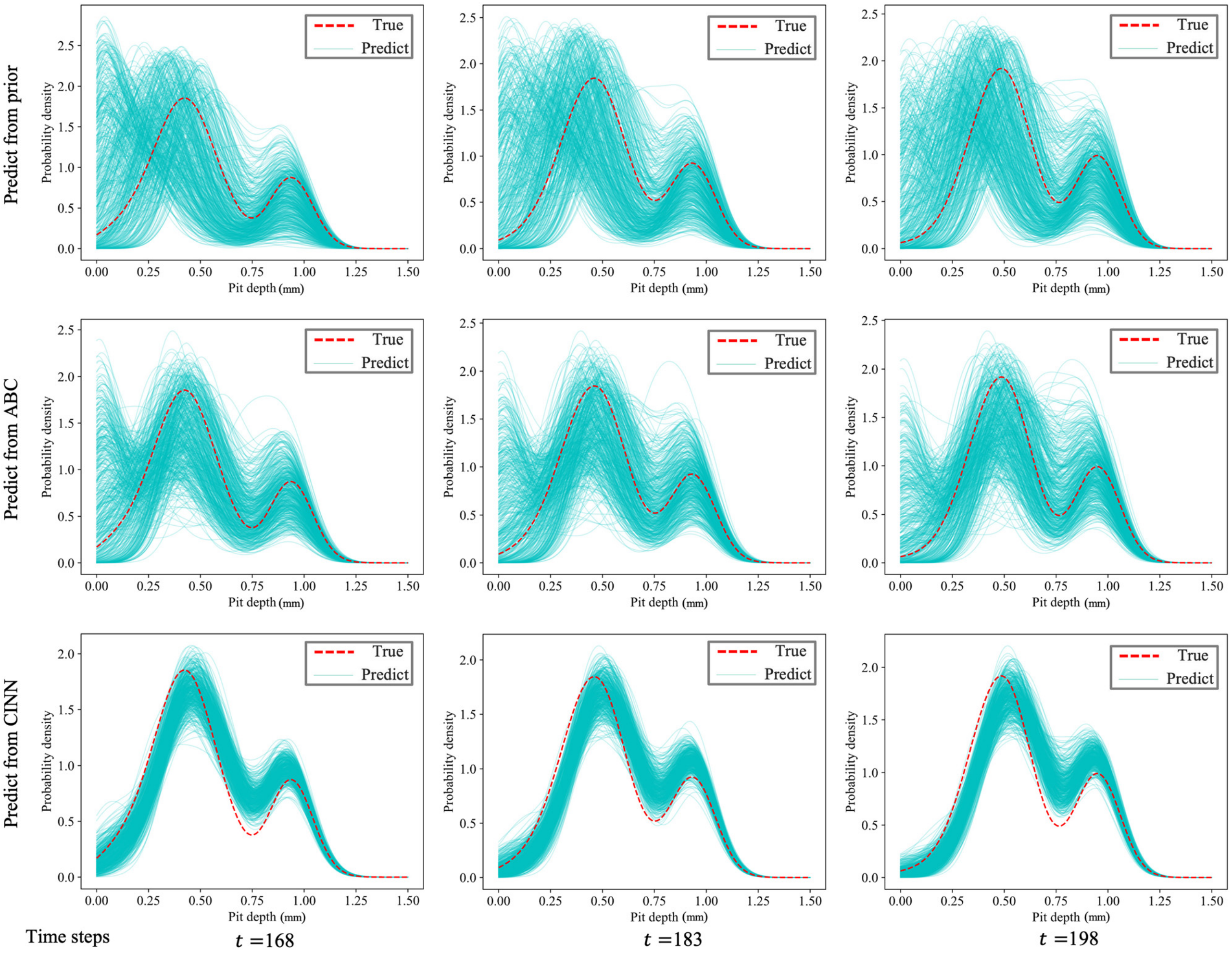

Fig. 12 Depth prediction results from the updated corrosion model parameters

Table 2 Comparison of computational cost between cINN and ABC

| | cINN | | ABC |
|---|---|---|---|
| | Training (h) | Inference (s) | Inference (h) |
| Time cost | 5 | 4 | 4 |

reference value, there are still considerable variance in the distribution. In summary, the cINN inference has more clear and plausible posterior distribution because it seems to gain more information than ABC approach.

After inferring from the observation of pit opening width, parameters are updated to predict future corrosion opening width. Figure 11 presents the prediction results of opening width. Each subplot illustrates the PDF of the opening width distribution at a specific time point. The reference PDF is depicted by the dashed line. In the first row, the prediction results from the prior samples exhibit a notable variance. Moving to the second row, predictions derived from ABC inference results show a reduction in variance. However, in the third row, predictions from cINN inference results demonstrate significantly enhanced accuracy and reduced variance compared to that from ABC. Despite this, both prediction results show decreasing accuracy over time. This is attributed to the inference process only providing current damage information. Near-future predictions, as evidenced by the 168th step, are more accurate compared to further-future predictions, as seen in the 198th step. It is essential to note that the plotted prediction results are based on observations from a static time point, specifically the 165th step. This is different from the dynamic Bayesian model updating which updates the model over time as new observations are incorporated.

With the physics-based multiscale simulation, pith depth is also able to be predicted with the updated parameters. Figure 12 shows the depth distribution prediction results. Similarly, the variance of prediction from cINN is smaller than that from ABC. However, the true value always lies in ABC prediction while sometimes lies outside the cINN prediction. This indicates that cINN sometimes is over confident about its prediction.

### 5.5 Discussion.

The notable difference in the inference outcomes likely stems from the variance in inference methodologies. A critical distinction between cINN and ABC lies in their respective approaches. A cINN effectively learns the relationship between simulation outcomes and parameters by employing a summary network and an inference network. The inference process in a cINN operates in the inverse direction of the trained invertible neural network. Conversely, ABC does not delve into this relationship; it merely accepts or rejects the current sample based on a threshold determined by human judgment. Significant uncertainties arise from varying judgments. Moreover, the posterior distribution from ABC hinges on the density of posterior samples across the entire parameter space, which is still subject to human judgment, thereby influencing the inference results.

Table 2 compares the computational cost between cINN and ABC. It is observed that computation cost for inference decreases from hours to seconds for cINN approach. This is because that ABC heavily depends on a “reject-accept” mechanism, where the

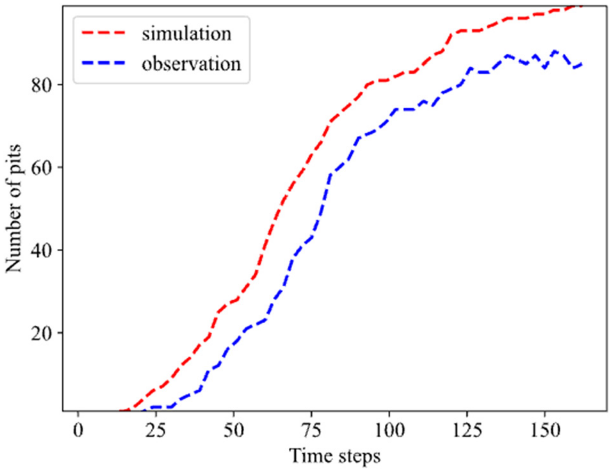

**Fig. 13 Observation bias in pit number**

user-defined tolerance level critically influences the accuracy of parameter estimation. Additionally, ABC requires rerunning its entire process for new datasets, a task that is computationally intensive. On the other hand, cINN operates without the necessity for a predefined threshold to estimate posterior samples, which generally leads to more consistent performance than ABC. More importantly, the cINN framework enables amortized inference where the computational expense is prepaid during offline training. This means that once training is finalized, the model can perform inferences on new datasets in a matter of seconds. This is a significant contrast to ABC, which require computations to be conducted from the ground up for each new dataset. The efficiency and accuracy of cINN, owing to its reduced need for computational resources during the inference phase, render it particularly advantageous and robust for practical applications.

In summary, cINN improves the efficiency and accuracy of Bayesian model updating for corrosion prognostics from three main aspects: (1) cINN directly learns the bijective relationships between latent variables and uncertain parameters, conditioned on observable quantities of interest. The posteriors of model parameters are estimated by sampling from the latent Gaussian distribution and applying a learned invertible mapping, conditional on observations. Unlike ABC, cINN does not rely on assumptions about prior or posterior distributions, nor does it require user-specified thresholds. This flexibility contributes to more reliable parameter estimates. (2) The proposed framework for model updating incorporates a complementary summary network, which is designed for automatic feature extraction and data compression. Utilizing a summary network is advantageous for handling high-dimensional data and addressing the unreliability associated with hand-crafted summary statistics used in other likelihood-free inference methods, such as ABC. (3) The proposed model updating framework enables amortized inference by incorporating a computationally intensive training phase upfront, followed by a rapid inference phase. This allows the framework to estimate parameters for any new dataset within seconds. In contrast, ABC necessitates rerunning the entire process from scratch for each new dataset, significantly reducing inference efficiency.

While the cINN approach offers advantages in terms of inference variance and computing efficiency, it encounters challenges related to the discrepancy between observation and simulation. This discrepancy arises from training the network on simulation data but applying it to infer based on observation data. Any biases in the observation can thus influence the inference outcomes, potentially leading to over-confidence. For instance, the inference results for $\theta$ exhibit a bias toward larger values than the reference for both the cINN and ABC approaches. This bias may be attributed to the detectability limit for small pits. If a pit is too small to be identified in the observation, there may be a delay in its detection, as also evidenced in $\beta$. The observation bias in pit number is shown in Fig. 13. We can clearly see that the observed pit number is constantly smaller than the simulation.

We further plot the observation bias in pit width distribution as shown in Fig. 14. There is a constant bias in observed pit width distribution versus the reference distribution at different observation times. This bias/delay in identifying the initiation of pits can result in a faster growth rate to match the pit width identified later, thereby leading to a larger reaction coefficient $\theta$ in the inference results. Importantly, the inference algorithm is not inherently aware of this bias. However, if the observation bias or uncertainty can be quantified, the cINN approach has the capability to propagate this uncertainty and compensate for the bias. For example, a correction term can be introduced to amend this bias. In this study, this aspect is not addressed due to limitations in the availability of observation data. Other sources might lead to bias, including the accuracy of pit width extraction, the angle and distance of picture-taking, lighting conditions, and obstacles covering the metal surface, such as failed protective paint or corrosion byproducts. Detailed cross-validation might be helpful in addressing these biases, ensuring more reliable and accurate model updating.

## 6 Conclusion

In summary, the cINN demonstrates impressive efficiency and accuracy when employed for Bayesian model updating in physics-based multiscale corrosion simulations. Such complex corrosion model can be inferred and updated within seconds for the first time. The cINN can significantly reduce the variance in inference compare to other likelihood-free approach like ABC. Sometimes the cINN might be overconfident about its inference results when there is observation bias. The future work would target minimizing/compensating such bias in the LFI approach. Advanced feature extraction techniques using computer vision may reduce observation bias, enhancing our ability to extract features from real images despite environmental noise. Moreover, quantifying the uncertainties stemming from observation bias could aid in compensating for

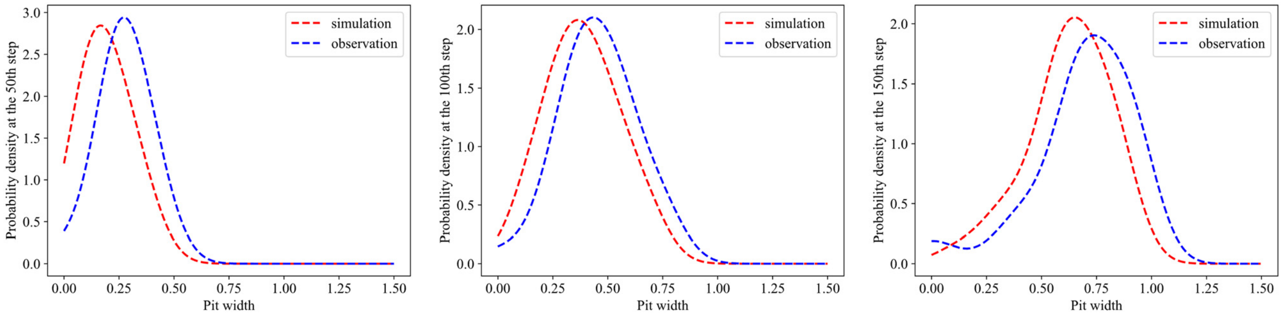

**Fig. 14 Observation bias in pit width distribution**

this bias. Additionally, efforts can be directed toward enhancing current simulator-based LFI techniques to address observation bias more effectively.

## Acknowledgment

Funding for this work was provided by the U.S. Army Corps of Engineers through the U.S. Army Engineer Research and Development Center Research Cooperative. The support is gratefully acknowledged.

## Funding Data

- Engineer Research and Development Center Research Cooperative (Agreement Nos. W9132T-22-20014 and W9132T-22-20014; Funder ID: 10.13039/100006505).

## Data Availability Statement

The datasets generated and supporting the findings of this article are obtainable from the corresponding author upon reasonable request.

## References

[1] Valdez, B., Ramirez, J., Eliezer, A., Schorr, M., Ramos, R., and Salinas, R., 2016, "Corrosion Assessment of Infrastructure Assets in Coastal Seas," J. Mar. Eng. Technol., **15**(3), pp. 124–134.

[2] Peng, L., Stewart, M. G., and Melchers, R. E., 2017, "Corrosion and Capacity Prediction of Marine Steel Infrastructure Under a Changing Environment," Struct. Infrastruct. Eng., **13**(8), pp. 988–1001.

[3] Yu, X., Wan, F., and Guo, Y., 2016, "Micromechanics Modeling of Skin Panel With Pitting Corrosion for Aircraft Structural Health Monitoring," IEEE International Conference on Prognostics and Health Management (ICPHM), Ottawa, ON, Canada, June 20–22, pp. 1–8.

[4] Burns, J., Larsen, J., and Gangloff, R., 2011, "Driving Forces for Localized Corrosion-to-Fatigue Crack Transition in Al–Zn–Mg–Cu," Fatigue Fract. Eng. Mater. Struct., **34**(10), pp. 745–773.

[5] Co, N. E. C., and Burns, J. T., 2021, "Effects of Micro-Scale Corrosion Damage Features and Local Microstructure on Fatigue Crack Initiation Location," Int. J. Fatigue, **150**, p. 106301.

[6] McDowell, D., and Dunne, F., 2010, "Microstructure-Sensitive Computational Modeling of Fatigue Crack Formation," Int. J. Fatigue, **32**(9), pp. 1521–1542.

[7] Jones, K., Hoeppner, D. W., and Dean, S. W., 2006, "Effect of Microstructure on Pit-to-Crack Transition of 7075-T6 Aluminum Alloy," J. ASTM Int., **3**(7), p. 100485.

[8] Chookah, M., Nuhi, M., and Modarres, M., 2011, "A Probabilistic Physics-of-Failure Model for Prognostic Health Management of Structures Subject to Pitting and Corrosion-Fatigue," Reliab. Eng. Syst. Saf., **96**(12), pp. 1601–1610.

[9] Ge, B., and Kim, S., 2021, "Probabilistic Service Life Prediction Updating With Inspection Information for RC Structures Subjected to Coupled Corrosion and Fatigue," Eng. Struct., **238**, p. 112260.

[10] Shekari, E., Khan, F., and Ahmed, S., 2017, "Probabilistic Modeling of Pitting Corrosion in Insulated Components Operating in Offshore Facilities," ASCE-ASME J. Risk Uncertainty Eng. Syst. Part B: Mech. Eng., **3**(1), p. 011003.

[11] Qian, G., Tantratian, K., Chen, L., Hu, Z., and Todd, M. D., 2022, "A Probabilistic Computational Framework for the Prediction of Corrosion-Induced Cracking in Large Structures," Sci. Rep., **12**(1), p. 20898.

[12] Qian, G., 2023, "Diagnostics and Prognostics of Pitting Corrosion in Large Civil Infrastructure Using Multi-Scale Simulation and Machine Learning," Ph.D. thesis, University of California San Diego, La Jolla, CA.

[13] Qian, G., Najera-Flores, D., Hu, Z., and Todd, M. D., 2023, "A Hybrid Surrogate Modeling Method for Corrosion Morphology Prediction Under Non-Stationary Dynamic Loading," Proceedings of the Structural Health Monitoring 2023, Stanford, CA, Sept. 12–14, pp. 643–650.

[14] Kayser, J. R., 1988, "The Effects of Corrosion on the Reliability of Steel Girder Bridges," Ph.D. thesis, University of Michigan, Ann Arbor, MI.

[15] Stewart, M. G., and Al-Harthy, A., 2008, "Pitting Corrosion and Structural Reliability of Corroding RC Structures: Experimental Data and Probabilistic Analysis," Reliab. Eng. Syst. Saf., **93**(3), pp. 373–382.

[16] Zhang, W., Zhou, B., Gu, X., and Dai, H., 2014, "Probability Distribution Model for Cross-Sectional Area of Corroded Reinforcing Steel Bars," J. Mater. Civ. Eng., **26**(5), pp. 822–832.

[17] Stewart, M. G., and Suo, Q., 2009, "Extent of Spatially Variable Corrosion Damage as an Indicator of Strength and Time-Dependent Reliability of RC Beams," Eng. Struct., **31**(1), pp. 198–207.

[18] Castaldo, P., Palazzo, B., and Mariniello, A., 2017, "Effects of the Axial Force Eccentricity on the Time-Variant Structural Reliability of Aging RC Cross-Sections Subjected to Chloride-Induced Corrosion," Eng. Struct., **130**, pp. 261–274.

[19] Akpanyung, K., and Loto, R., 2019, "Pitting Corrosion Evaluation: A Review," J. Phys.: Conf. Ser., **1378**(2), p. 022088.

[20] Gong, C., and Frangopol, D. M., 2020, "Reliability of Steel Girder Bridges With Dependent Corrosion Growth," Eng. Struct., **224**, p. 111125.

[21] Saassouh, B., and Lounis, Z., 2012, "Probabilistic Modeling of Chloride-Induced Corrosion in Concrete Structures Using First-and Second-Order Reliability Methods," Cem. Concr. Compos., **34**(9), pp. 1082–1093.

[22] Shi, P., and Mahadevan, S., 2003, "Corrosion Fatigue and Multiple Site Damage Reliability Analysis," Int. J. Fatigue, **25**(6), pp. 457–469.

[23] Scheiner, S., and Hellmich, C., 2007, "Stable Pitting Corrosion of Stainless Steel as Diffusion-Controlled Dissolution Process With a Sharp Moving Electrode Boundary," Corros. Sci., **49**(2), pp. 319–346.

[24] Stafiej, J., Di Caprio, D., and Bartosik, Ł., 2013, "Corrosion-Passivation Processes in a Cellular Automata Based Simulation Study," J. Supercomput., **65**(2), pp. 697–709.

[25] Zhang, G., Gazonas, G. A., and Bobaru, F., 2018, "Supershear Damage Propagation and Sub-Rayleigh Crack Growth From Edge-On Impact: A Peridynamic Analysis," Int. J. Impact Eng., **113**, pp. 73–87.

[26] Chen, L.-Q., 2002, "Phase-Field Models for Microstructure Evolution," Annu. Rev. Mater. Res., **32**(1), pp. 113–140.

[27] Zeng, J., Kim, Y. H., and Qin, S., 2023, "Bayesian Model Updating for Structural Dynamic Applications Combing Differential Evolution Adaptive Metropolis and Kriging Model," J. Struct. Eng., **149**(6), p. 04023070.

[28] Kitahara, M., Bi, S., Broggi, M., and Beer, M., 2021, "Bayesian Model Updating in Time Domain With Metamodel-Based Reliability Method," ASCE-ASME J. Risk Uncertainty Eng. Syst., Part A: Civ. Eng., **7**(3), p. 04021030.

[29] Beaumont, M. A., Zhang, W., and Balding, D. J., 2002, "Approximate Bayesian Computation in Population Genetics," Genetics, **162**(4), pp. 2025–2035.

[30] Csilléry, K., Blum, M. G., Gaggiotti, O. E., and François, O., 2010, "Approximate Bayesian Computation (ABC) in Practice," Trends Ecol. Evol., **25**(7), pp. 410–418.

[31] Toni, T., Welch, D., Strelkowa, N., Ipsen, A., and Stumpf, M. P., 2009, "Approximate Bayesian Computation Scheme for Parameter Inference and Model Selection in Dynamical Systems," J. R. Soc., Interface, **6**(31), pp. 187–202.

[32] Wood, S. N., 2010, "Statistical Inference for Noisy Nonlinear Ecological Dynamic Systems," Nature, **466**(7310), pp. 1102–1104.

[33] Gutmann, M. U., Dutta, R., Kaski, S., and Corander, J., 2018, "Likelihood-Free Inference Via Classification," Stat. Comput., **28**(2), pp. 411–425.

[34] Ardizzone, L., Kruse, J., Wirkert, S., Rahner, D., Pellegrini, E. W., Klessen, R. S., Maier-Hein, L., Rother, C., and Köthe, U., 2019, "Analyzing Inverse Problems With Invertible Neural Networks," The Seventh International Conference on Learning Representations (ICLR), New Orleans, LA, May 6–9.

[35] Kobyzev, I., Prince, S. J., and Brubaker, M. A., 2021, "Normalizing Flows: An Introduction and Review of Current Methods," IEEE Trans. Pattern Anal. Mach. Intell., **43**(11), pp. 3964–3979.

[36] Ardizzone, L., Lüth, C., Kruse, J., Rother, C., and Köthe, U., 2019, "Guided Image Generation With Conditional Invertible Neural Networks," e-print arXiv:1907.02392.

[37] Bister, T., Erdmann, M., Köthe, U., and Schulte, J., 2022, "Inference of Cosmic-Ray Source Properties by Conditional Invertible Neural Networks," Eur. Phys. J. C, **82**(2), pp. 1–10.

[38] Zeng, J., Todd, M. D., and Hu, Z., 2023, "Probabilistic Damage Detection Using a New Likelihood-Free Bayesian Inference Method," J. Civ. Struct. Health Monit., **13**(2–3), pp. 319–341.

[39] Zeng, J., Todd, M. D., and Hu, Z., 2023, "A Recursive Inference Method Based on Invertible Neural Network for Multi-Level Model Updating Using Video Monitoring Data," Mech. Syst. Signal Process., **203**, p. 110736.

[40] Padmanabha, G. A., and Zabaras, N., 2021, "Solving Inverse Problems Using Conditional Invertible Neural Networks," J. Comput. Phys., **433**, p. 110194.

[41] Qian, G., Hu, Z., and Todd, M. D., 2023, "Physics-Based Corrosion Reliability Analysis of Miter Gates Using Multi-Scale Simulations and Adaptive Surrogate Modeling," Mech. Syst. Signal Process., **200**, p. 110619.

[42] Najera-Flores, D. A., Qian, G., Hu, Z., and Todd, M. D., 2023, "Corrosion Morphology Prediction of Civil Infrastructure Using a Physics-Constrained Machine Learning Method," Mech. Syst. Signal Process., **200**, p. 110515.

[43] Gutman, E. M., 1994, *Mechanochemistry of Solid Surfaces*, World Scientific Publishing Company, Singapore.

[44] Gutman, E. M., 1998, *Mechanochemistry of Materials*, Cambridge International Science Publishing, Cambridge, UK.

[45] Li, T., Wu, J., and Frankel, G., 2021, "Localized Corrosion: Passive Film Breakdown versus Pit Growth Stability, Part VI: Pit Dissolution Kinetics of Different Alloys and a Model for Pitting and Repassivation Potentials," Corros. Sci., **182**, p. 109277.

[46] Tokuda, S., Muto, I., Sugawara, Y., and Hara, N., 2020, "Pit Initiation on Sensitized Type 304 Stainless Steel Under Applied Stress: Correlation of Stress, Cr-Depletion, and Inclusion Dissolution," Corros. Sci., **167**, p. 108506.

[47] Zhang, W., Brown, B., Young, D., and Singer, M., 2021, "Pitting Mechanism of Mild Steel in Marginally Sour Environments—Part II: Pit Initiation Based on the Oxidation of the Chemisorbed Iron Sulfide Layers," Corros. Sci., **184**, p. 109337.

[48] Tokuda, S., Muto, I., Sugawara, Y., and Hara, N., 2021, "The Role of Applied Stress in the Anodic Dissolution of Sulfide Inclusions and Pit Initiation of Stainless Steels," Corros. Sci., **183**, p. 109312.

[49] Suter, T., Webb, E. G., Böhni, H., and Alkire, R. C., 2001, "Pit Initiation on Stainless Steels in 1 m Nacl With and Without Mechanical Stress," J. Electrochem. Soc., **148**(5), p. B174.

[50] Frankel, G. S., Li, T., and Scully, J. R., 2017, "Perspective–Localized Corrosion: Passive Film Breakdown versus Pit Growth Stability," J. Electrochem. Soc., **164**(4), pp. C180–C181.

[51] Ascher, H., and Feingold, H., 1984, *Repairable Systems Reliability: Modeling, Inference, Misconceptions and Their Causes*, Marcel Dekker, New York.

[52] Li, X., Zhao, Y., Qi, W., Wang, J., Xie, J., Wang, H., Chang, L., et al., 2019, "Modeling of Pitting Corrosion Damage Based on Electrochemical and Statistical Methods," J. Electrochem. Soc., **166**(15), pp. C539–C549.

[53] Eick, B. A., Treece, Z. R., Spencer, B. F., Jr., Smith, M. D., Sweeney, S. C., Alexander, Q. G., and Foltz, S. D., 2018, "Automated Damage Detection in Miter Gates of Navigation Locks," Struct. Control Health Monit., **25**(1), p. e2053.

[54] Vega, M. A., Hu, Z., Yang, Y., Chadha, M., and Todd, M. D., 2022, "Diagnosis, Prognosis, and Maintenance Decision Making for Civil Infrastructure: Bayesian Data Analytics and Machine Learning," *Structural Health Monitoring Based on Data Science Techniques*, Springer, New York.

[55] Qian, G., Wu, Z., Hu, Z., and Todd, M. D., 2024, "Pitting Corrosion Monitoring Framework for Miter Gates with Digital Twin," Proceedings of the 11th European Workshop on Structural Health Monitoring, Potsdam, Germany, June 10–13.

[56] Gourieroux, C., Monfort, A., and Renault, E., 1993, "Indirect Inference," J. Appl. Econometrics, **8**(S1), pp. S85–S118.

[57] Sisson, S. A., Fan, Y., and Tanaka, M. M., 2007, "Sequential Monte Carlo Without Likelihoods," Proc. Natl. Acad. Sci., **104**(6), pp. 1760–1765.

[58] Park, J.-K., Kwon, B.-K., Park, J.-H., and Kang, D.-J., 2016, "Machine Learning-Based Imaging System for Surface Defect Inspection," Int. J. Precis. Eng. Manuf.-Green Technol., **3**(3), pp. 303–310.

[59] Yun, J. P., Shin, W. C., Koo, G., Kim, M. S., Lee, C., and Lee, S. J., 2020, "Automated Defect Inspection System for Metal Surfaces Based on Deep Learning and Data Augmentation," J. Manuf. Syst., **55**, pp. 317–324.

[60] Radev, S. T., Mertens, U. K., Voss, A., Ardizzone, L., and Köthe, U., 2022, "Bayesflow: Learning Complex Stochastic Models With Invertible Neural Networks," IEEE Trans. Neural Networks Learn. Syst., **33**(4), pp. 1452–1466.

[61] Dinh, L., Sohl-Dickstein, J., and Bengio, S., 2017, "Density Estimation Using Real NVP," The Fifth International Conference on Learning Representation (ICLR), Toulon, France, Apr. 24–26.

[62] Foltz, S. D., 2017, "Investigation of Mechanical Breakdowns Leading to Lock Closures," ERDC-CERL Champaign United States, Report No. TR-17-17, Vicksburg, MI.

[63] Kondo, Y., 1989, "Prediction of Fatigue Crack Initiation Life Based on Pit Growth," Corrosion, **45**(1), pp. 7–11.